Josephson effect through $YBa_2Cu_3O_{7-\delta}$/Au-encapsulated nanogaps

Reza Baghdadi,[1] Simon Abay,[2] Dmitri Golubev,[3] Thilo Bauch,[1] and Floriana Lombardi[1,*]

[1]*Quantum Device Physics Laboratory, Department of Microtechnology and Nanoscience, Chalmers University of Technology, 41296 Göteborg, Sweden*

[2]*Department of Solid State Physics, Lund University, Lund, Sweden*

[3]*Low Temperature Laboratory (OVLL), Aalto University School of Science, P.O. Box 13500, FI-00076 Aalto, Finland*

(Received 14 February 2017; published 17 May 2017)

We successfully fabricated and studied planar superconductor-normal-superconductor (SNS) Josephson junctions made of $YBa_2Cu_3O_{7-\delta}$ (YBCO) high-T_C superconductor (S) and Au normal metal (N). The crucial step in fabrication was done by using a Pt/Au bilayer encapsulation of the patterned YBCO nanogap. This procedure preserves the YBCO nanogap from the degradation due to the contact with resists, water, and chemicals involved in further processing for hybrid devices. The junctions exhibit Fraunhofer-like modulation patterns and Shapiro steps when they are irradiated by a rf field. Furthermore, we analyzed the $I_C(T)$ characteristics of our hybrid junctions employing a SINI′S (superconductor–insulator–normal conductor–insulator–superconductor) model.

DOI: 10.1103/PhysRevB.95.174510

I. INTRODUCTION

Nanotechnologies applied to high critical temperature superconductors (HTS) have paved the way to the realization of superconducting electronics with novel functionalities. Interesting theoretical reports, for example, make use of the *d*-wave symmetry of the order parameter in HTS and the large value of the superconducting gap to design experiments to reveal the existence of Majorana fermions, still elusive particles in solid state systems, that are supposed to nucleate at the interface between a superconductor and a topological insulator (TI) [1–3]. Majorana fermions, which are their own antiparticles, obey a non-Abelian statistics at the basis of topological quantum computation, which evades decoherence at the hardware level [4]. Another example is given by the realization of HTS devices interfaced with graphene. In such structures one could study the quantum Hall effect in a regime of Josephson transport, which is accessible because of the extremely high upper critical field of HTS (of the order of 100 T) and superconducting gap [5–7].

At the same time, superconductor-semiconductor interfaces have a broad potential for a wide range of applications. The use of HTS could bring several advantages, and more importantly higher operational temperatures fundamental for practical applications of superconducting field effect transistors [8–11].

The fabrication of HTS hybrid devices requires however the engineering of reproducible and stable nanogaps. This is a challenging task because of the surface and chemical instability of thin films and the very short superconducting coherence length ξ of the order of few nanometers ($\xi_{a,b} \approx 1$–2 nm and $\xi_c \approx 0.2$–0.3 nm). Previous attempts made use of high aspect ratio trenches excavated in perovskite substrates by various techniques [12]. The subsequent YBCO growth was expected to be discontinued at the trench top, resulting in the formation of a YBCO nanogap, which was bridged with Ag forming a superconductor (S)–normal metal (N)–superconductor (S) Josephson junction.

However, these approaches suffered from the random formation of grain boundaries along the trench profile, which could mimic the SNS behavior [13]. Moreover, the resulting YBCO nanogaps cannot be easily integrated with complex normal conductors, like for example flakes of TI/graphene or semiconducting nanowires, since the YBCO nanogap sides are exposed to ambient and would be seriously damaged once in contact to chemicals and resist for further processing.

In this paper, we show a flexible way to obtain $YBa_2Cu_3O_{7-\delta}$ nanogaps, which can be easily employed to realize HTS hybrid devices. Here, the basic concept is the complete Au encapsulation of the electrodes, forming the nanogap. This procedure allows one to preserve the properties of YBCO (close to the pristine film) in the closest proximity of the normal conductor. The feasibility of our nanogaps, for hybrid devices, has been tested by bridging the nanogaps with Au and by studying Josephson properties of the resulting S-N-S junctions.

II. DEVICE FABRICATION

The fabrication process of YBCO nanogap based SNS junctions involves three main electron beam lithography (EBL) steps which are schematically depicted in Figs. 1(a)–1(c). More details on the fabrication process can be found elsewhere [14]. Briefly, to realize our devices, first a nanogap structure is defined in a high-quality, epitaxial *c*-axis-oriented $YBa_2Cu_3O_{7-\delta}$ film grown on a (110) MgO substrate, with a thickness of 50 nm and covered with a 25 nm thick protective layer of Au (deposited *in situ*). The resist baking temperature is kept below 90 °C for all three lithography steps to minimize oxygen out diffusion from the film. The nanogaps are defined by using a combination of a diamondlike carbon (DLC) mask and soft ion milling [14–16]. The slope that the nanogap edges form with the substrate has been extracted by atomic force microscope (AFM) and scanning electron microscope (SEM) inspection of the nanostructures in analogy with previous works [17,18]. We get a slope angle of 75° as schematically shown in the cross section of Fig. 1(a).

To encapsulate the $YBa_2Cu_3O_{7-\delta}$/Au nanogaps including the side walls, a Pt/Au bilayer (5 nm/50 nm) is deposited

*floriana.lombardi@chalmers.se

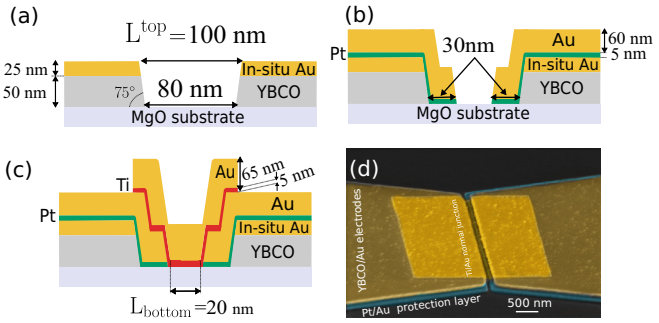

FIG. 1. Schematic sketch of the process flow to fabricate the encapsulated YBCO/Au/YBCO junctions. (a) Nanogap formation: the pattern is transferred by the EBL to a diamondlike carbon mask and then to the Au/YBCO films by Ar^+ ion milling. Here, the top lateral spacing between the electrodes is 100 nm (L^{top} = 100 nm) but due to the line edge roughness, intrinsic of e-beam lithography process, and the edge's slope, the spacing between two YBCO electrodes at the bottom of the trenches shrinks to 80 nm. (b) Encapsulation of the nanogap by patterning of the bilayer of Pt/Au (5 nm/60 nm). (c) Definition of the SNS junction. The distance L_{bottom} between the protected YBCO electrodes is about 20 nm. (d) SEM image of a final SNS junction.

by sputtering. A second EBL procedure is used to open again the nanogap using a transferred pattern slightly larger (20 to 40 nm) with respect to the original nanogaps. This design aims to properly cover with Pt/Au the edges of the nanogap [Fig. 1(b)]. The encapsulated YBCO nanostructures can be readily interfaced with exotic conductors like TI flakes, semiconducting nanowires, or graphene.

The third and the last EBL step is performed to define the geometry of the S-N-S junctions. Here, we have chosen as normal metal a Au film, so the third EBL step will define the geometry of the Au bridging the nanogap. This is done by using a lift-off process for a Ti (5 nm)/Au (65 nm) bilayer [Fig. 1(c)]. We used a 5 nm Ti film as the sticking layer between the Au and substrate to improve the adhesion. Junctions with a width of 2–3 μm and different nanogap top lengths L^{top} = 80, 100, and 120 nm have been analyzed. Here L^{top} is the top lateral spacing between the electrodes [see Fig. 1(a)].

Figure 1(d) shows a SEM image of a typical device. To recover the oxygen loss and damages occurring at the edges of the nanogap, in particular during the ion milling procedure to form the nanogaps, we preformed an *ex situ* ozone annealing [14,15] after the full process. This procedure has shown to be very effective to recover optimal doping in YBCO nanowires and to restore YBCO gap features at the YBCO/Pt/Au interfaces [14,15]. However, we cannot exclude that this procedure may lead to a formation of an oxide layer on the Ti adhesion film as we will discuss later.

III. TRANSPORT MEASUREMENTS AND DISCUSSION

We have characterized the transport properties of the SNS junctions. The measurements were performed in a ^{3}He cryostat with a base temperature of 300 mK.

For reasons that will be clear through the text we will discuss first the transport properties of nanogap based SNS junctions with L^{top} = 100 and 120 nm. The superconducting properties

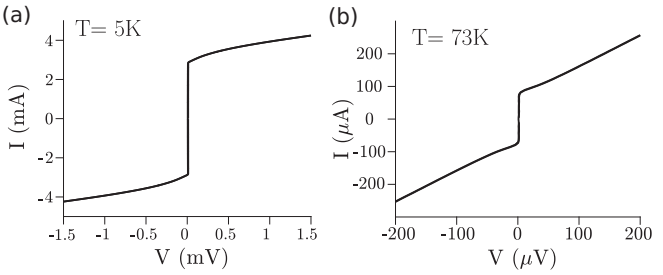

FIG. 2. Current-voltage characteristic of the junction (SNS no. 1) junction at (a) T = 5 K and (b) T = 73 K.

of the junctions were measured by recording the current voltage characteristics (IVC) as a function of temperature, magnetic field, and microwave irradiation.

Figure 2 shows a typical IVC at two different temperatures for the junction with nominal L^{top} = 100 nm and w = 2 μm ("SNS no. 1"). We get a critical current density J_C = 1.45 MA/cm^2 at T = 5 K and J_C = 38 k A/cm^2 at 73 K. We see a clear transition from a flux-flow-like behavior at very low temperature to a resistively shunted junction (RSJ) behavior close to the critical temperature of the device (T_C = 75 K). This phenomenology is often observed in magnetically long junctions when the Josephson penetration depth λ_J is much shorter than the width w [19]. For our specific planar type junctions, the Josephson penetration depth has to be calculated by considering nonlocal electrodynamics [20]. The nonlocal l_J and local λ_J [21] Josephson penetration depths are related by the expression $l_J = \lambda_J^2/\lambda_L = \Phi_0/4\pi\mu_0\lambda_L^2 J_C$. Here, Φ_0 is the flux quantum and λ_L is the London penetration depth in the a-b planes.

For the junction SNS no. 1 of Figs. 2(a) and 2(b), we get $l_j \sim 210$ nm at T = 5 K while increasing to about 1.5 μm at T = 73 K when the junction is closer to the magnetically short junction regime ($w \sim 2l_J$). By applying an external magnetic field normal to the film, we observe a Fraunhofer-like dependence of the Josephson current [21–23] as shown in Fig. 3. Due to the self-field effect, the magnetic pattern $I_C(B)$ of the junction at T = 68 K is slanted [Fig. 3(a)]. At higher temperatures, the SNS device behaves as a junction in the intermediate regime ($w \sim 4l_J$) and we observe a close to Fraunhofer-like dependence of the Josephson current at T = 74 K [21–23] as shown in Fig. 3(b).

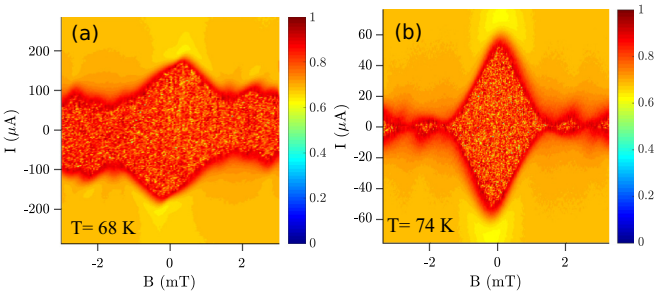

FIG. 3. Normalized logarithmic conductance map as a function of bias current and external magnetic field of the junction (SNS no. 1) with width w = 2 μm and L^{top} = 100 nm at temperatures (a) T = 68 K and (b) T = 74 K.

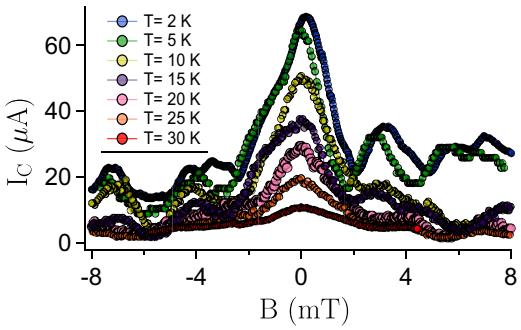

FIG. 4. Magnetic modulation of the critical current at a series of temperatures for the junction (SNS no. 2) with $w = 3\ \mu$m and $L^{\text{top}} = 120$ nm.

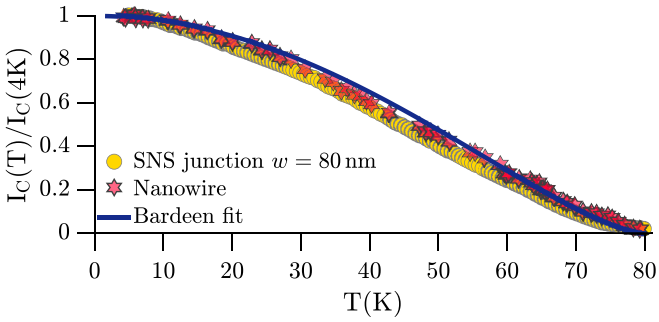

FIG. 5. Normalized critical current as a function of temperature for the junction (SNS no. 3) with $L^{\text{top}} = 80$ nm (yellow circles), a YBCO nanowire with $w = 90$ nm (red stars), and the Bardeen fit (blue solid line).

From the magnetic pattern [Fig. 3(b)] we get that the distance between two side lobes $\Delta B \sim 1$ mT is in good agreement with the predicted value $\Delta B \sim 1.84\Phi_0/w^2$ for thin-film planar junctions [24] considering $w \sim 2\ \mu$m.

The reason that the position of the first minimum in the $I_C(B)$ pattern is larger than the ΔB [Fig. 3(b)] is that the junction width w is comparable with l_J. In this limit, the influence of the current induced magnetic field is still important. We expect that the screening currents around the junction cause the critical current to decrease linearly with increasing the applied magnetic field as $I_C(B) = I_C(0)(1 - |B|/B_C)$ [19,25,26].

Figure 4 shows the evolution in temperature of the magnetic pattern for a junction with $w = 3\ \mu$m and $L^{\text{top}} = 120$ nm ("SNS no. 2"). We observe a Fraunhofer-like dependence in the all temperature range from 2 to 30 K. Because of the much reduced critical current density $J_C = 35$ k A/cm^2 at 5 K, due to the longer nanogap, one gets $l_J = 1.55\ \mu$m, close to the width of the junction already at the lowest temperature. Also in this case from the measured $\Delta B \approx 2.7$ mT one extracts an effective width $\approx 1.18\ \mu$m of the junction not too far from the geometrical one.

To get more insight into the transport regime in our junctions we have studied the behavior of the Josephson current as a function of the temperature. Here, we consider an SINI'S model [27] on the basis of the Gor'kov equations. We assume that the two barriers at the left and right YBCO/Au interfaces [Fig. 1(b)] have transparencies $\mathcal{T}_1$ and $\mathcal{T}_2$, respectively.

The Josephson current can be evaluated from the following expression [27]:

$$I_J(\varphi) = \frac{8ek_BT}{\hbar}\frac{k_F^2 wh}{4\pi}\sin\varphi \sum_{\omega_n>0}\int_0^1 d\mu\,\mu\,\frac{t_1t_2}{\sqrt{Q(\varphi,\mu)}}, \quad (1)$$

where $t_{1,2} = \mathcal{T}_{1,2}/(2 - \mathcal{T}_{1,2})$ are the barrier strengths and Q reads as

$$Q(\varphi,\mu) = \left[t_1t_2\cos\varphi + \left(1 + (1+t_1t_2)\frac{\hbar^2\omega_n^2}{\Delta^2}\right)\cosh[2\omega_n t_0(\mu)] + (t_1+t_2)\frac{\hbar^2\Omega_n\omega_n}{\Delta^2}\sinh[2\omega_n t_0(\mu)]\right]^2 - \left(1-t_1^2\right)\left(1-t_2^2\right)\frac{\hbar^4\Omega_n^4}{\Delta^4}, \quad (2)$$

where e is the elementary charge, l_e is the mean free path of the N layer, Δ is the superconducting order parameter, $\omega_n = \pi k_B T(2n+1)/\hbar$ are the Matsubara frequencies, $\hbar\Omega_n = \sqrt{\hbar^2\omega_n^2 + \Delta^2}$, h is the thickness of the normal metal, w is the junction's width, and L is the distance between the electrodes.

In Eq. (2), $\mu = \sin\theta$, where θ is the angle between the speed of the electrons and the line normal to the leads edges. Therefore, $t_0(\mu)$ is the time of flight of electrons moving along the straight line connecting the two YBCO leads having the angle θ and takes the form

$$t_0(\mu) = \frac{l_e}{(1-\mu^2)\left(\sqrt{1+\frac{l_e^2}{L^2(1-\mu^2)}}-1\right)}. \quad (3)$$

In the clean junction limit, $l_e = \infty$, $t_0(\mu)$ reads

$$t_0(\mu) = \frac{L}{v_F\sqrt{1-\mu^2}}. \quad (4)$$

In the diffusive limit t_0 does not depend on μ and becomes

$$t_0 = \frac{2L^2}{v_F l_e}. \quad (5)$$

The normal state resistance of the junction is given by

$$R_N = \frac{\pi\hbar}{e^2}\frac{4\pi}{k_F^2 wh}\left(\frac{1}{\mathcal{T}_1}+\frac{1}{\mathcal{T}_2}+\frac{3L}{4l_e}-1\right). \quad (6)$$

Let's first consider the $I_C(T)$ of a YBCO/Au/YBCO junction with a very short inner-electrode distance. In Fig. 5, we present the temperature dependence of the normalized critical current $I_C(T)$ of an SNS junction with $L^{\text{top}} = 80$ nm and $w = 3\ \mu$m ("SNS no. 3"). For comparison, we also show the normalized $I_C(T)$ of a nanowire with $W = 90$ nm, where W is the width of the nanowire. Both curves can be well fitted using the Bardeen approximation in the full range of temperature below T_C, $I_C \propto [1-(T/T_C)^2]^{3/2}$ [28], which usually holds for nanowires [29]. This evidence leads us to conclude that the electrodes forming the YBCO nanogap are possibly shortened. Here we discuss plausible scenarios which could be responsible for the occurrence of these shorts.

As a result of Ar ion milling, necessary to fabricate YBCO nanogaps, the sidewalls of YBCO electrodes have a finite slope. In Fig. 1(c) we have shown that this effect together with the unavoidable line edge roughness due to e-beam lithography procedure, result in a distance of the electrodes, in the bottom

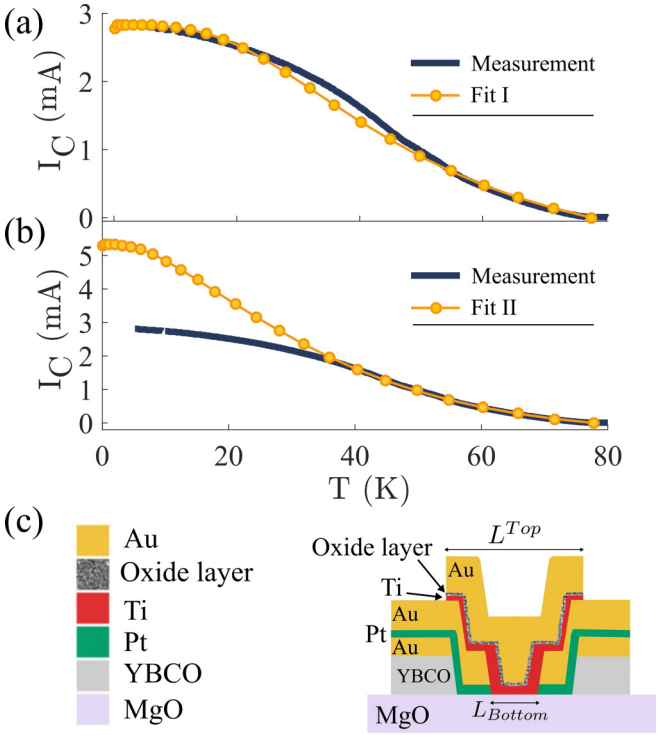

FIG. 6. Measured (blue line) and theoretical (yellow circles) critical current vs temperature for the encapsulated YBCO-Au-YBCO junction (SNS no. 1) using fitting parameters I (a) and II (b) from Table I. (c) Cross section of a SNS junction. Because of the ozone treatment on our SNS junctions, it is plausible that a very thin oxide is formed at the Ti/Au interface. The oxide layer makes the transport of Cooper pairs more desirable through the Ti layer.

of the trench of approximately 20 nm for nominal nanogap of $L^{\text{top}} = 100$ nm. It is therefore quite possible that nanogaps with nominal $L^{\text{top}} = 80$ nm are shortened at the bottom.

This tiny leftover YBCO layer can be the result of a high aspect ratio system where the width of the gap is only half of the initial YBCO/Au thickness.

Figure 6 shows the critical current as a function of the temperature for the SNS no. 1 device ($L^{\text{top}} = 100$ nm), which is characterized by the $I_C(B)$ presented in Fig. 3. To fit the $I_C(T)$ measurement with Eq. (1), we assumed a value $\Delta \approx 16.5$ meV for the superconducting energy gap at the interface YBCO/Au in agreement with what we have found experimentally [14] and what is reported in literature [30]. As many parameters are involved in the SINI′S model, there is not a unique set that can fit our data (see Table I).

A rather good agreement between our data and the theoretical dependence is obtained by assuming two different transparencies at the SN interfaces [Fig. 6(a)]. From the fitting (see parameters for the Fit I in Table I), we learn that the proximity current is through the thin Ti layer which we employed as a sticking layer. Indeed the extracted thickness h of the bridging normal metal is the same as the thickness of the Ti film. The obtained junction length L is comparable with the one estimated at the bottom edge of the nanogap L_{bottom} [see Fig. 1(c)]. This scenario could be due to the ozone treatment on our junction. Even though the ozone treatment is needed and is expected to improve the degraded YBCO layer at the interface, on the other hand, it could be responsible for the formation of a very thin oxide at the Ti layer [see Fig. 6(c)]. Because of this extra barrier, the Cooper pair transport is more favorable through the Ti in contact with the substrate.

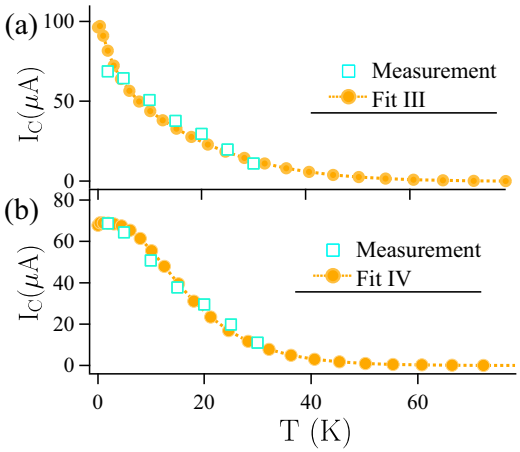

FIG. 7. Measured (cyan squares) and theoretical (yellow circles) critical current vs temperature for the encapsulated YBCO-Au-YBCO junction SNS no. 2 using fitting parameters III (a) and IV (b) from Table II.

Although this fit looks very promising, we need to consider also other aspects. First, the huge discrepancy in the interface transparency values $\mathcal{T}_1$ and $\mathcal{T}_2$ cannot be easily justified considering the fabrication process. Moreover, we don't expect any good theoretical fit at low temperatures. This is because the junction is in the long junction limit at low temperatures, which is reflected by the slanted magnetic pattern [see Fig. 3(a)]. This is an indication that the junction behaves more like an asymmetric in-line junction [21]. Although our SNS junction doesn't have an in-line configuration, the small value of l_J at low temperatures together with possible nonuniformity of the interface transparency may result in an inhomogeneous J_C which makes the junction emulate an in-line behavior. It is known that, in this regime, the critical current is saturated for $w > 4l_J$ [19,21] and I_C does not scale anymore with the junction width w.

Considering these facts, we have fitted the high-temperature region of the $I_C(T)$ dependence by considering quite trans-

TABLE I. Fitting parameters used in the fits I and II for the junction (SNS no. 1).

	L (nm)	w (nm)	h (nm)	$\mathcal{T}_1$	$\mathcal{T}_2$	Δ_0 (meV)	T_C (K)	l_e (nm)
Fit (I)	11.5	500	5	0.18	1	16.5	77.8	5
Fit (II)	13	500	5	0.55	0.55	16.5	77.8	5

TABLE II. Fitting parameters used in the fits III and IV for the junction (SNS no. 2).

	L (nm)	w (nm)	h (nm)	$\mathcal{T}_1$	$\mathcal{T}_2$	Δ_0 (meV)	T_C (K)	l_e (nm)
Fit III	17	500	5	0.09	0.09	16.5	77.8	5
Fit IV	20	500	5	0.0122	1	16.5	77.8	5

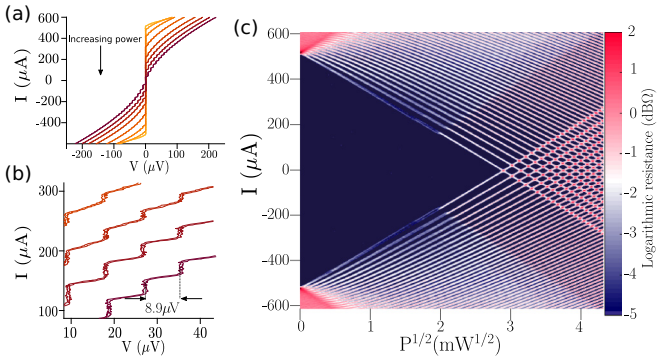

FIG. 8. (a) Current-voltage characteristic of the YBCO-Au-YBCO junction (SNS no. 1) with $w = 2\ \mu$m and $L^{\text{top}} = 100$ nm, taken at $T = 65$ K for 4.34 GHz rf radiation at various microwave powers. (b) Shapiro steps with a distance in voltage of $\Delta V = hf/2e = 8.9\ \mu V$ are clearly observed. (c) The logarithmic differential resistance dV/dI of the same junction is plotted as a function of the applied rf-power and the junction's current I for $f = 4.43$ GHz.

parent and identical interfaces [see Fig. 6(b)]. The obtained parameters for this fit are listed in Table I (Fit II). The fit is reasonable in the high-temperature regime where the junction is in the short limit. The higher expected theoretical values of I_C, compared with the experimental ones at low temperatures, supports the fact that the junction is in long junction limit and it is not possible to fit the $I_C(T)$ measurements in the low-temperature regime. Furthermore, also in this case we get that the Cooper pair transport is through the Ti layer and that the length of the junction is comparable to what is expected from geometrical considerations.

Figure 7 shows the $I_C(T)$ dependence for the junction SNS no. 2 ($L^{\text{top}} = 120$ nm). For this junction, we considered the same T_C value as for the junction (SNS no. 1). Two sets of fitting parameters are listed in Table II. Using $L \approx 17$ nm and $h = 5$ nm (see Fit III in Table II), we get a good agreement between experiment and theory by considering identical transparencies. The extracted value of the thickness h reinforces the argument that the leading transport channel is through the 5 nm thick Ti layer at the interface with the substrate. Furthermore, comparing the obtained length for the junction SNS no. 1 (Table I), the increase in the L to about 20 nm (Table II) is in line with the fact that the top length L^{top} is 20 nm larger for SNS no. 2. Also for this junction a reasonable fit can be obtained by considering asymmetric barriers' transparencies (see Fit IV in Table II).

We have studied the ac-Josephson effect in our SNS junctions by radiating microwaves through a coaxial waveguide which is terminated by an antenna about 10 mm above the sample.

As a result of the synchronization of the Josephson frequency with a microwave radiation frequency, f, Shapiro steps appear at specific voltages $V_n = nhf/2e$ in the IV characteristics [31]. Here, h is the Planck's constant, e is the elementary charge, f is the microwave frequency, and $n = 0, \pm 1, \pm 2, \ldots$.

Figure 8(a) shows the measured IVCs of the SNS junction (SNS no. 1) with $w = 2\ \mu$m and $L^{\text{top}} = 100$ nm, placed under microwave irradiation of different powers at $f = 4.34$ GHz. Voltage spacing between the Shapiro steps is measured as $\Delta V = 8.9\ \mu$V, which is consistent with the expected value $\Delta V = hf/2e = 8.97\ \mu$V. A logarithmic differential resistance map as a function of current and the microwave amplitude is shown in Fig. 8(b). The triangularlike modulation of the current steps is most probably related to the fact that the junction is current biased and that the applied microwave frequency f is much smaller than the $I_C R_n/\Phi_0$ product of our junction [32].

IV. CONCLUSION

To conclude, we have demonstrated a versatile fabrication process to develop YBCO nanogaps which can potentially be implemented in HTS hybrid devices. This is achieved by encapsulating the sidewalls of patterned YBCO nanogaps with a Pt/Au bilayer. To verify that the encapsulation method preserves the superconducting properties of the YBCO structures, we fabricated and characterized YBCO-Au-YBCO SNS junctions.

The magnetic field dependence of the Josephson critical current I_C showed at high temperature a Fraunhofer-like pattern which is expected for SNS junctions with a uniform current distribution. Besides, under microwave irradiation, we also observed Shapiro steps in the current-voltage characteristics of our junctions.

By using a double barrier SINI′S model, we have studied the transport properties of the critical current in temperature. The results of the fitting suggest that the Cooper pair transport is mainly across the 5 nm Ti sticking layer due to the ozone treatment. This circumstance should be considered for further implementation of this nanogap in complex devices.

This study provides a promising technological basis for making HTS hybrid devices to study a variety of novel phenomena, which are expected to arise in such systems.

ACKNOWLEDGMENTS

This work has been partially supported by the Swedish Research Council (VR) and by the Swedish Foundation for Strategic Research (SSF) under the project "Graphene based high-frequency electronics". R.B. is supported by a grant from the Area of Advance Nano. Clean-room processing has been achieved using equipment sponsored by the Knut and Alice Wallenberg Foundation.

[1] A. C. Potter and L. Fu, Phys. Rev. B **88**, 121109 (2013).
[2] P. Zareapour, A. Hayat, S. Y. F. Zhao, M. Kreshchuk, Y. K. Lee, A. A. Reijnders, A. Jain, Z. Xu, T. S. Liu, G. D. Gu, S. Jia, R. J. Cava, and K. S. Burch, Phys. Rev. B **90**, 241106(R) (2014).
[3] J. Linder, Y. Tanaka, T. Yokoyama, A. Sudbø, and N. Nagaosa, Phys. Rev. Lett. **104**, 067001 (2010).
[4] C. Nayak, S. H. Simon, A. Stern, M. Freedman, and S. Das Sarma, Rev. Mod. Phys. **80**, 1083 (2008).

[5] Y. Zhang, Y.-W. Tan, H. L. Stormer, and P. Kim, Nature (London) **438**, 201 (2005).
[6] A. Tzalenchuk, S. Lara-Avila, A. Kalaboukhov, S. Paolillo, M. Syväjärvi, R. Yakimova, O. Kazakova, J. J. B. M., V. Fal'ko, and S. Kubatkin, Nat. Nanotechnol. **5**, 186 (2010).
[7] P. Rickhaus, M. Weiss, L. Marot, and C. Schönenberger, Nano Lett. **12**, 1942 (2012).
[8] D. E. McCumber, J. Appl. Phys. **39**, 2503 (1968).
[9] J. Mannhart, Supercond. Sci. Technol. **9**, 49 (1996).
[10] F. Tafuri and J. R. Kirtley, Rep. Prog. Phys. **68**, 2573 (2005).
[11] F. Tafuri, D. Massarotti, L. Galletti, D. Stornaiuolo, D. Montemurro, L. Longobardi, P. Lucignano, G. Rotoli, G. P. Pepe, A. Tagliacozzo, and F. Lombardi, J. Supercond. Novel Magn. **26**, 21 (2013).
[12] R. P. Robertazzi, A. W. Kleinsasser, R. B. Laibowitz, R. H. Koch, and K. G. Stawiasz, Phys. Rev. B **46**, 8456 (1992).
[13] P. Lucignano, D. Stornaiuolo, F. Tafuri, B. L. Altshuler, and A. Tagliacozzo, Phys. Rev. Lett. **105**, 147001 (2010).
[14] R. Baghdadi, R. Arpaia, S. Charpentier, D. Golubev, T. Bauch, and F. Lombardi, Phys. Rev. Appl. **4**, 014022 (2015).
[15] R. Baghdadi, R. Arpaia, T. Bauch, and F. Lombardi, IEEE Trans. Appl. Supercond. **25**, 1100104 (2015).
[16] R. Arpaia, S. Nawaz, F. Lombardi, and T. Bauch, IEEE Trans. Appl. Supercond. **23**, 1101505 (2013).
[17] S. Nawaz, R. Arpaia, F. Lombardi, and T. Bauch, Phys. Rev. Lett. **110**, 167004 (2013).
[18] S. Charpentier, R. Arpaia, J. Gaudet, D. Matte, R. Baghdadi, T. Löfwander, D. Golubev, P. Fournier, T. Bauch, and F. Lombardi, Phys. Rev. B **94**, 060503 (2016).
[19] A. Barone, W. J. Johnson, and R. Vaglio, J. Appl. Phys. **46**, 3628 (1975).
[20] A. A. Boris, A. Rydh, T. Golod, H. Motzkau, A. M. Klushin, and V. M. Krasnov, Phys. Rev. Lett. **111**, 117002 (2013).
[21] A. Barone and G. Paterno, *Physics and Applications of the Josephson Effect* (Wiley-Interscience Publication, New York, 1982).
[22] J. M. Rowell, Phys. Rev. Lett. **11**, 200 (1963).
[23] M. Tinkham, *Superconductivity*, Documents on Modern Physics: Gordon and Breach (Gordon and Breach, New York, 1966).
[24] P. A. Rosenthal, M. R. Beasley, K. Char, M. S. Colclough, and G. Zaharchuk, Appl. Phys. Lett. **59**, 3482 (1991).
[25] C. S. Owen and D. J. Scalapino, Phys. Rev. **164**, 538 (1967).
[26] B. Mayer, S. Schuster, A. Beck, L. Alff, and R. Gross, Appl. Phys. Lett. **62**, 783 (1993).
[27] A. V. Galaktionov and A. D. Zaikin, Phys. Rev. B **65**, 184507 (2002).
[28] J. Bardeen, Rev. Mod. Phys. **34**, 667 (1962).
[29] S. Nawaz, R. Arpaia, T. Bauch, and F. Lombardi, Phys. C (Amsterdam, Neth.) **495**, 33 (2013).
[30] A. Sharoni, I. Asulin, G. Koren, and O. Millo, Phys. Rev. Lett. **92**, 017003 (2004).
[31] S. Shapiro, Phys. Rev. Lett. **11**, 80 (1963).
[32] P. Russer, J. Appl. Phys. **43**, 2008 (1972).